European Heart Journal – Cardiovascular Imaging (2017) **17**, 19–30
doi:10.1093/ehjci/jew048

Combined non-invasive assessment of endothelial shear stress and molecular imaging of inflammation for the prediction of inflamed plaque in hyperlipidaemic rabbit aortas

Gitsios Gitsioudis[1†*], Yiannis S. Chatzizisis[2,3,4†*], Peter Wolf[1], Anna Missiou[1], Antonios P. Antoniadis[3,4], Dimitrios Mitsouras[5], Sönke Bartling[6], Zeynep Arica[1], Matthias Stuber[7,8], Frank J. Rybicki[5], Max Nunninger[1], Christian Erbel[1], Peter Libby[4], George D. Giannoglou[3], Hugo A. Katus[1], and Grigorios Korosoglou[1]

[1]Department of Cardiology, University of Heidelberg, Heidelberg, Germany; [2]Cardiovascular Division, University of Nebraska Medical Center, Omaha, Nebraska, USA; [3]First Department of Cardiology, AHEPA University Hospital, Aristotle University Medical School, Thessaloniki, Greece; [4]Cardiovascular Division, Brigham and Women's Hospital, Harvard Medical School, Boston, Massachusetts, USA; [5]Department of Radiology, Brigham and Women's Hospital, Harvard Medical School, Boston, Massachusetts, USA; [6]Medical Physics in Radiology, German Cancer Research Center, Heidelberg, Germany; [7]Russell H. Morgan Department of Radiology and Radiological Sciences, Division of MR Research, Johns Hopkins University School of Medicine, Baltimore, Maryland, USA; and [8]Center for Biomedical Imaging, University Hospital Lausanne, Lausanne, Switzerland

Received 29 December 2015; accepted after revision 21 February 2016; online publish-ahead-of-print 24 March 2016

Aims To evaluate the incremental value of low endothelial shear stress (ESS) combined with high-resolution magnetic resonance imaging (MRI)- and computed tomography angiography (CTA)-based imaging for the prediction of inflamed plaque.

Methods and results Twelve hereditary hyperlipidaemic rabbits underwent quantitative analysis of plaque in the thoracic aorta with 256-slice CTA and USPIO-enhanced (ultra-small superparamagnetic nanoparticles, P904) 1.5-T MRI at baseline and at 6-month follow-up. Computational fluid dynamics using CTA-based 3D reconstruction of thoracic aortas identified the ESS patterns in the convex and concave curvature subsegments of interest. Subsegments with low baseline ESS exhibited significant increase in wall thickness and plaque inflammation by MRI, in non-calcified plaque burden by CTA, and developed increased plaque size, lipid and inflammatory cell accumulation (high-risk plaque features) at follow-up by histopathology. Multiple regression analysis identified baseline ESS and inflammation by MRI to be independent predictors of plaque progression, while receiver operating curve analysis revealed baseline ESS alone or in combination with inflammation by MRI as the strongest predictor for augmented plaque burden and inflammation (low ESS at baseline: AUC = 0.84, $P < 0.001$; low ESS and inflammation by molecular MRI at baseline: AUC = 0.89, $P < 0.001$).

Conclusion Low ESS predicts progression of plaque burden and inflammation as assessed by non-invasive USPIO-enhanced MRI. Combined non-invasive assessment of ESS and imaging of inflammation may serve to predict plaque with high-risk features.

Keywords atherosclerosis • hyperlipidaemic rabbits • endothelial shear stress • molecular imaging • magnetic resonance imaging • computed tomography angiography

* Corresponding author. Tel: +49 6221 56 4130; Fax: +49 6221 56 5513. E-mail: gitsioudis_correspondence@web.de (G.G.); Tel: +1 402 559 5156; Fax: +1 402 559 8355. E-mail: ychatzizisis@icloud.com (Y.S.C.)

† The first two authors contributed equally to this study.

Translational perspective

Prior investigations highlighted low ESS as an important determinant of plaque development and progression. Yet, little evidence exists on the role of low ESS in the identification of lesions that may progress rapidly and develop inflammation associated with precipitating clinical events. Since the diameter of the rabbit aortas resembles that of human coronary arteries, our findings have potential for translation to humans. This study validates a multimodality non-invasive approach of combined local haemodynamic patterns with phagocytic activity for the prediction of inflamed plaque. The combination of local ESS, which favours ongoing inflammation with the severity of inflammation, may serve to identify high-risk plaques, thereby targeting pre-emptive systemic or even local treatments that may alter the natural history of atherosclerosis. Furthermore, our study highlights the potential of multimodality non-invasive longitudinal monitoring of high-risk plaque to assess the effect of novel therapies.

Introduction

Non-invasive identification and prediction of atherosclerotic plaque with high-risk characteristics remains a difficult challenge. Inflammation indubitably influences the pathogenesis of high-risk plaques.[1–3] Lesions that provoke fatal myocardial infarctions plaque often display increased wall thickness, luminal irregularities, and high lipid and macrophage but low calcium content.[4,5] Experimental studies have shown that low endothelial shear stress (ESS) associates strongly with inflammation and lipid accumulation, promoting atherogenesis, plaque formation, and progression to vulnerability.[6–8] However, limited data exist on the role of ESS for plaque evolution derived from serial non-invasive imaging studies.

Non-invasive imaging can identify different plaque constituents. High-resolution magnetic resonance imaging (MRI) with ultra-small superparamagnetic nanoparticles (USPIOs) can identify plaque inflammation[9] and assess disease progression.[10–12] Plaque macrophages phagocytize USPIOs detectable by MRI using dedicated off-resonance sequences.[9,13–17] Computed tomography angiography (CTA), on the other hand, can visualize regions of low attenuation or spotty calcification,[18,19] characteristic that associated with prospective risk of acute coronary syndromes.[20–24]

Conceptually, a combined assessment of ESS and inflammation may have incremental value for the identification of high-risk plaque. This experimental study investigated the hypothesis that combined non-invasive calculation of ESS by CTA and imaging of inflammation by USPIO-enhanced MRI can predict the development of inflamed plaque. These experiments used genetically hyperlipidaemic rabbits, animals that develop inflamed macrophage-rich aortic plaques.

Methods

Study animals and design

The study was approved by the Institutional Animal Care and Use Committee. Experiments were conducted in 12 male heritable hyperlipidaemic Watanabe WHHL-MI rabbits (2.2–3.2 kg body weight), which received ketamine (50 mg/kg) and xylazine (20 mg/kg) intramuscularly for general anaesthesia during all imaging studies. *Table 1* shows the characteristics of study animals. All rabbits consumed a normal chow diet; they appeared healthy and active throughout the study period and had normal life span.

The animals underwent MRI (before and after USPIO injection) and CTA at baseline (age: 7.5 ± 0.1 months) and at follow-up (age: 13.0 ± 0.2 months) (*Figure 1*). ESS in the thoracic aorta was assessed non-invasively at baseline via computational fluid dynamics (CFD) using 3D reconstructions of the aortic lumen from contrast-enhanced CT angiography. At the end of the study, animals underwent euthanasia using an overdose of thiopental. The aortas were then isolated and analysed histopathologically for inflammation, lipids, and calcification.

Serial MRI studies

MRI studies were performed with a clinical 1.5 T system (Achieva, Philips Healthcare, Best, The Netherlands) using a 32-element cardiac phased-array receiver coil. The detailed imaging protocol is provided in the Supplementary data online. For the assessment of plaque inflammation, we performed high-resolution off-resonance MRI using USPIO as contrast material (250 μmol Fe/Kg; P904 provided by Guerbet, Villepinte, France), as previously described.[9] A dedicated off-resonance MRI sequence (Inversion Recovery with ON-Resonant water suppression, IRON-MRI) evaluated the regional USPIO uptake by the macrophages, as previously described.[9] Animals were imaged with MRI immediately before the USPIO injection and 4 days later[9] (*Figure 1*).

Serial CTA studies

CTA images were acquired using a clinical 256-slice CT scanner (iCT, Philips Medical Systems, Best, The Netherlands) immediately after the molecular MRI (*Figure 1*). A standardized retrospective electrocardiogram-gated protocol focused on anatomical high-resolution visualization of the aortic vessel was applied. The detailed imaging protocol is provided in the Supplementary data online.

3D reconstruction of aortas and CFD at baseline

Aortic CTA acquisitions were routinely reconstructed at the diastolic phase (75% phase). This image data set was segmented from aortic valve to the infrarenal level, along with the major branches (right and left innominate and renal arteries). At baseline, the aortas (from the aortic valve to the infrarenal level) along with the major branches (right and left innominate and renal arteries) underwent multiplanar reformatting and semi-automatic segmentation using a clinical image post-processing workstation (Vitrea 6.4, Vital Images, A Toshiba Medical Systems Group, Minnetonka, MN, USA). Customized software developed in Matlab (Matlab R2013a, Mathworks, Natick, MA, USA) permitted creation of a 3D mesh of the reconstructed arterial volumes. The mesh consisted of tetrahedral elements plus five prismatic layers close to the wall to capture near-wall effects.

The baseline ESS was calculated from the aorta 3D mesh representations *using a commercially* available CFD software (*Fluent 15, ANSYS Inc., PA, USA)* (*Figure 2A*). The inlet velocity of each reconstructed aorta at the level of the aortic valve was calculated by the ratio of blood flow assessed by 2D velocity-encoding phase-contrast MRI over the aortic valve area. *Flow was considered as 3D, steady, laminar, isothermal with no external forces applied on it, and the arterial wall was assumed to be non-elastic and impermeable. Blood was assumed to obey a non-Newtonian power law model and to have constant density. ESS distribution was*

Table 1 Characteristics of the study animals ($n = 12$) at baseline and follow-up

Parameters	Baseline	Follow-up	P
Age (months)	7.5 ± 0.1	13.0 ± 0.2	<0.001
Weight (kg)	2.75 ± 0.1	2.81 ± 0.1	ns
Triglycerides (mg/dL)	305 ± 22	224 ± 26	0.02
Total cholesterol (mg/dL)	944 ± 30	870 ± 33	ns
HDL (mg/dL)	15 ± 3	12 ± 2	ns
LDL (mg/dL)	886 ± 33	806 ± 27	ns
VLDL (mg/dL)	136 ± 51	103 ± 51	ns
Leukocytes (cells/nL)	3.9 ± 0.4	4.1 ± 0.4	ns
Thrombocytes (cells/nL)	383 ± 35	421 ± 23	ns
Hs-CRP (mg/dL)	<2.0	<2.0	ns
Hs-TnT (pg/mL)	6.8 ± 1.2	10.7 ± 2.2	ns
Creatinine (mg/dL)	0.68 ± 0.02	0.61 ± 0.0.03	0.04
Urea (mg/dL)	43.0 ± 1.9	37.9 ± 1.1	0.03
GOT (U/L)	27.0 ± 2.4	32.6 ± 4.7	ns
GPT (U/L)	67.7 ± 4.5	80.1 ± 7.2	ns

Hs-TnT, high-sensitive troponin T; Hs-CRP, high-sensitive C-reactive protein; HDL, high-density lipoprotein; LDL, low-density lipoprotein; VLDL, very-low-density lipoprotein; GOT, glutamic oxaloacetic transaminase; GPT, glutamic pyruvate transaminase.

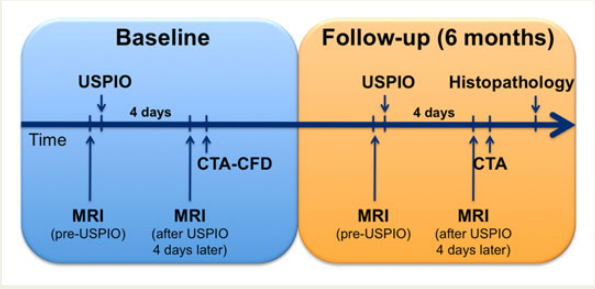

Figure 1 Experimental study design: serial MRI with and without contrast, CTA, and CFD studies performed at baseline and follow-up in hereditary hyperlipidaemic rabbits.

represented using 2D maps with arterial length (mm) in the x-axis and artery circumference (degrees) in the y-axis (*Figure 2B*).

Identification of convex (outer curvature) and concave (inner curvature) wall subsegments of interest at baseline

All analyses were performed in the thoracic portion of the aorta. The reconstructed aortas were divided into 5-mm-long segments. In the ascending aorta and aortic arch, all sequential segments were analysed, whereas in the thoracic aorta we selected two to three representative segments. To account for the circumferential (convex vs. concave wall) heterogeneity in ESS patterns across a given aorta, each 5-mm-long segment was further divided into the convex curvature subsegment, extending clockwise from −60 to +60°, and the concave curvature subsegment extending clockwise from +120 to −120° (*Figure 2A*). The longitudinal line across the convex curvature passing through the middle of the ostium of the right innominate was set as 0°.

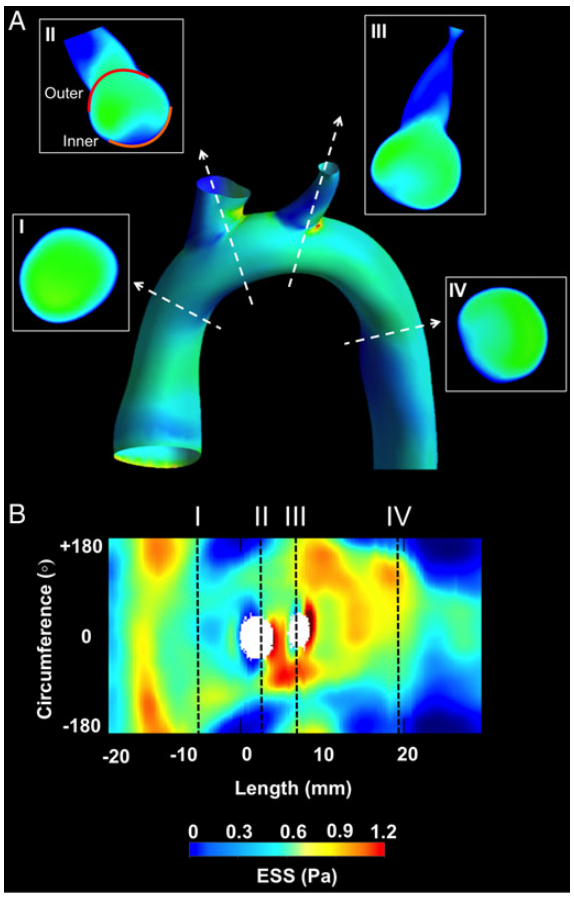

Figure 2 Representative example of CFD in a 3D reconstructed aorta: (*A*) 3D reconstructed aorta and proximal parts of major branches and ESS distribution by CFD. Representative cross-sections (I–IV) at the level of the ascending aorta, aortic arch, and descending aorta. Using the take-off of right innominate artery as reference (0°), the outer (convex) 120° (II, red line) and inner (concave) 120° (II, orange line) were identified in each cross-section. (*B*) 2D map representation of ESS distribution; *y*-axis represents the vessel circumference and *x*-axis the vessel length. Cross-sections (I–IV) in (*A*) correspond to the black dashed lines. The ostia of the major aortic arch branches are also shown.

The average ESS was calculated in the convex and concave subsegments. To account for the inter-aorta ESS heterogeneity, the average ESS in each subsegment was classified into low, moderate, and high based on the frequency distribution of ESS values in each aorta: (i) low ESS subsegment if average ESS ≤25th percentile of the frequency distribution, (ii) intermediate ESS subsegment if average ESS between 25th and 75th percentile of the frequency distribution, and (iii) high ESS subsegment if average ESS ≥75th percentile of the frequency distribution.

Longitudinal and circumferential co-registration of imaging modalities, CFD, and histopathology

For longitudinal-axis co-registration of pre-USPIO MRI, post-USPIO MRI, CTA, CFD, and histopathology, we identified the most proximal

point of the ostium of the right innominate artery as a fixed anatomical landmark and set it as 0 mm. To identify and match the convex and concave curvature in each modality and in histology, we used the longitudinal line of the convex curvature passing through the middle of the ostium of the right innominate and we set it as 0°.

Aortic wall thickness and inflammation by MRI

The aortic wall thickness was measured in cross-sections corresponding to the middle of 5-mm-long segments using pre-contrast black-blood turbo field echo MR images (BB-TFE-MRI) at baseline and follow-up as previously described (Soapbubble software tool, release 5.1 for PRIDE V4.*+V5, Philips Healthcare, Best, The Netherlands).[25] The USPIO concentration-dependent image contrast ratio, an indication of inflammation in the aortic wall, was calculated using the normalized enhancement ratio (NER) according to the following formula as previously described:[9,26]

$$\mathrm{NER} = \frac{(\mathrm{SNR}_{\mathrm{WALL-Post-Contrast}}/\mathrm{SNR}_{\mathrm{BLOOD-Post-Contrast}})}{(\mathrm{SNR}_{\mathrm{WALL-Pre-Contrast}}/\mathrm{SNR}_{\mathrm{BLOOD-Pre-Contrast}})},$$

where SNR corresponded to the signal-to-noise-ratio in regions of interest placed in the aortic wall and the adjacent aortic lumen in the pre- and post-USPIO images.[9] The matching between the pre- and post-USPIO images used fiducial landmarks, including the aortic bulb, supra-aortic branches, and the vertebral bodies. Increased vessel wall enhancement was indicated by a NER of >1. Two blinded experts performed all measurements of the aortic wall thickness and NER.

Aortic wall analysis by CTA

Quantitative aortic wall analysis in CTA was performed with Plaque SW 4.0.2 (Extended Brilliance Workspace 4.0, Philips Medical Systems, Best, The Netherlands) and Osirix MD v 2.8 (Osirix, Pixmeo Sarl, Bernex, Switzerland) at baseline and follow-up. The Supplementary data online provides a detailed description of the software-assisted plaque evaluation. Two blinded experts performed the CTA-based wall analysis.

Histopathology

Histopathological analysis was performed to assess the plaque area (mm^2), calcification (calcified area over plaque area, %), lipids (lipid area over plaque area, %), and macrophages (macrophage area over plaque area, %). Supplementary data online provides a detailed description of the histopathological analysis, which were performed by two blinded experts.

Statistical analyses

Statistical analyses were performed with MedCalc 15.2.2 (MedCalc Software, Mariakerke, Belgium), IBM SPSS Statistics 21.0 (IBM Corp., New York, NY, USA) for mixed-effects analysis and with Graph Pad Prism version 5 (GraphPad Software, La Jolla, CA, USA). Continuous variables were summarized as mean $\pm$ standard error of mean (SEM) and categorical variables as actual numbers and percentages. Several statistical methods corrected for systematic error introduced by the clustering of aortic subsegments within animals. First, investigation of the association of continuous dependent variables (e.g. increase of NER, wall thickness, and macrophage content) with categorical independent variables (e.g. baseline ESS) used mixed-effects one-way analysis of variance (ANOVA) with the animals specified as random effects and with *post hoc* Scheffé test for pairwise comparisons. Second, the association of continuous variables used mixed-effects linear regression with the animals specified as random effects. The Huber White sandwich estimator adjusted the SEs of the regression coefficient for clustering of arterial subsegments within animals in linear regression and logistic regression analyses. In linear prediction models, linear model validity was tested using the Cusum test. A receiver operating curve (ROC) analysis assessed the predictive value of baseline ESS and baseline NER for the development of macrophage- and lipid-rich plaques as validated by histopathological examination. The inter- and intra-observer (8 weeks apart) agreement of MRI and CTA measurements used Pearson's correlation, coefficient linear regression analysis, and Bland–Altman analysis in a representative sample of 20 images. *P*-value of ≤ 0.05 was considered as the level of statistical significance.

Results

All study animals completed the follow-up. All animals had MRI at baseline and follow-up. For technical reasons, four rabbits did not undergo baseline CTA, but all animals had follow-up CTA.

Baseline ESS

A total of 88 concave wall and convex wall subsegments were identified. Three subsegments ($n = 3$) were excluded from final analysis due to reduced image quality in MRI. At baseline, the concave wall subsegments had predominantly low ESS, whereas convex wall subsegments had higher ESS (*Figure 2A*). This pattern of circumferential ESS distribution was most evident in the aortic arch and descending thoracic aorta.

Association of low baseline ESS with wall thickness increase by MRI

Wall thickness change over time assessed via serial BB-TFE-MRI at baseline and at follow-up showed that at baseline, regions with low ESS exhibited significantly greater wall thickness compared with regions with intermediate or high ESS (0.69 ± 0.02 vs. 0.61 ± 0.02 vs. 0.63 ± 0.03 mm, $P = 0.016$ for low vs. intermediate ESS; *Figure 3A*). At follow-up, regions with low baseline ESS had a significant increase of wall thickness compared with regions with intermediate or high baseline ESS (follow-up to baseline wall thickness ratio: 13.0 ± 2.1 vs. 4.6 ± 0.8 vs. 6.1 ± 1.0%, $P = 0.006$ for low vs. intermediate baseline ESS, and for low vs. high baseline ESS, *Figure 3B–F*). The increase in wall thickness in subsegments with low baseline ESS exceeded the intra- and inter-observer variability of wall thickness measurements by MRI (1.1 ± 1.8 and 1.6 ± 2.0%, respectively).

Association of low baseline ESS with plaque burden at follow-up by CTA

Non-calcified plaque area and volume at follow-up were 1.8- and 2.4-fold higher in regions of low vs. high baseline ESS (plaque area: 1.68 ± 0.13 vs. 0.95 ± 0.05 mm^2, $P < 0.001$; plaque volume: 2.14 ± 0.21 vs. 0.91 ± 0.07 mm^3, $P < 0.001$; *Figure 4A* and *B*). *Figure 4C–F* demonstrates representative examples of ESS distribution in 3D reconstructed aortas (*Figure 4C* and *E*) and the corresponding reformatted CTA images (*Figure 4D* and *F*) of the aorta at follow-up showing higher plaque burden in regions with low baseline ESS compared with high ESS.

Association of low baseline ESS with high-risk plaque features determined by histopathological analysis

All animals were sacrificed immediately after the 6-month follow-up MRI and CTA imaging and underwent histopathological study of the

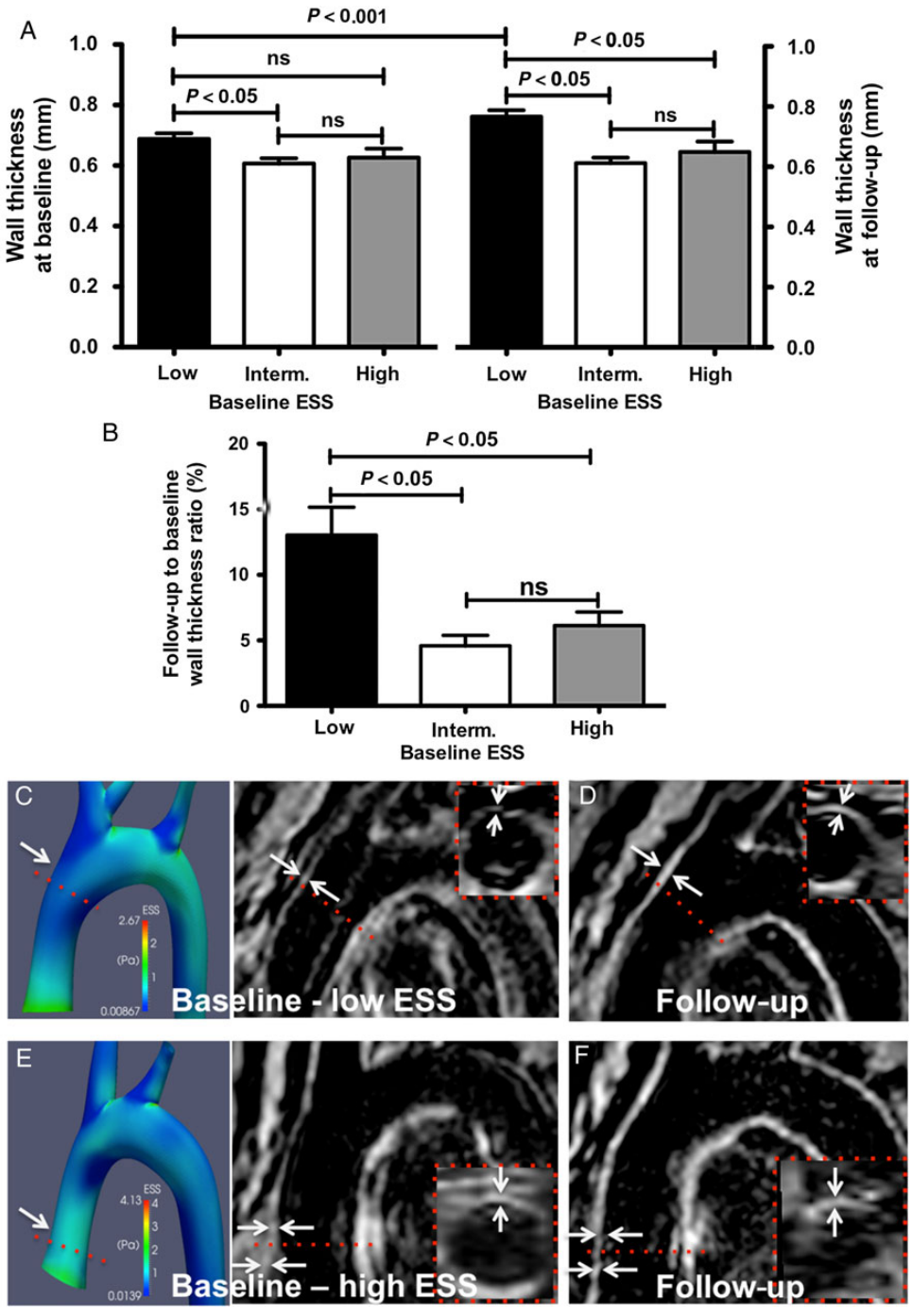

Figure 3 Wall thickness analysis by non-contrast MRI: (*A*) increased wall thickness at baseline and follow-up in subsegments with low baseline ESS compared with subsegments with intermediate or high ESS. (*B*) Subsegments with low baseline ESS exhibited augmented increase in wall thickness compared with intermediate or high ESS. (*C*–*F*) Representative examples of 3D reconstructed aortas and MRI images at baseline showing increased wall thickness (*D*, arrows, dashed lines and inserts) in regions with low ESS (*C*) at baseline vs. regions with high ESS (*E* and *F*).

concave and convex wall subsegments of interest. In line with the MRI and CTA findings, subsegments with low ESS at baseline developed significantly higher plaque area compared with high and intermediate ESS subsegments as assessed histopathologically (3.7 $\pm$ 0.3 vs. 2.4 $\pm$ 0.2 vs. 2.2 $\pm$ 0.2 mm^2, $P < 0.001$ for low vs. intermediate ESS and for low vs. high ESS; *Figure 5A* and *C*). Similarly, baseline subsegments with low ESS displayed significantly higher lipid and macrophage content than regions with intermediate and high ESS at baseline (lipids: 14.2 $\pm$ 1.0 vs. 9.8 $\pm$ 1.1 vs. 6.8 $\pm$ 1.5%, $P < 0.001$ for low vs. intermediate ESS and for low vs. high ESS; *Figure 5B*

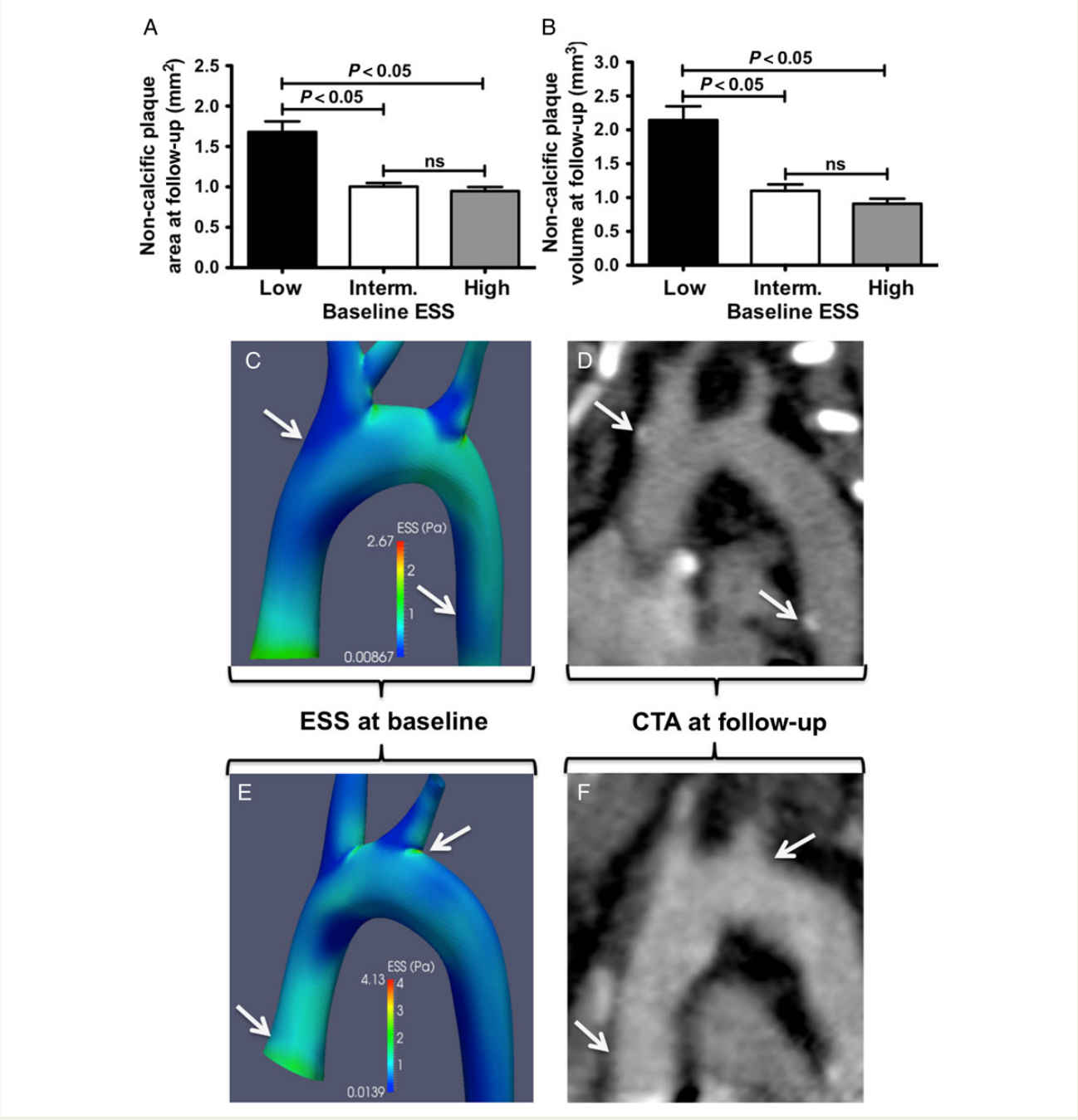

Figure 4 Wall thickness analysis by CTA: increased non-calcified plaque area (*A*) and plaque volume (*B*) at follow-up in subsegments with low baseline ESS compared with intermediate or high ESS. (*C*–*F*) Representative examples of ESS distribution in 3D reconstructed aortas at baseline (*C* and *E*) and the corresponding multiplanar reformatted aortas at follow-up (*D* and *F*). Regions with low baseline ESS (*C*, arrows) exhibited increased plaque burden by CTA (*D*, arrows indicate mixed plaques) compared with subsegments with high ESS (*E* and *F*, arrows).

and *D*; macrophages: 9.4 ± 0.8 vs. 5.3 ± 0.8 vs. 4.4 ± 1.1%, $P < 0.001$ for low vs. intermediate ESS and for low vs. high ESS; *Figure 5E* and *G*). Finally, subsegments of low baseline ESS exhibited greater calcification than subsegments with intermediate or high ESS as determined histopathologically (6.3 ± 0.8 vs. 3.0 ± 0.4 vs. 2.2 ± 0.7%, $P < 0.001$ for low vs. intermediate ESS and for low vs. high ESS; *Figures 4C–F* and *5F* and *H*).

Association of low baseline ESS with inflammation progression by molecular MRI

Serial IRON-MRI before and after the administration of USPIO at baseline and at 6 months showed quantifiable changes in signal intensity within the aortic wall by NER. Specifically, NER at follow-up

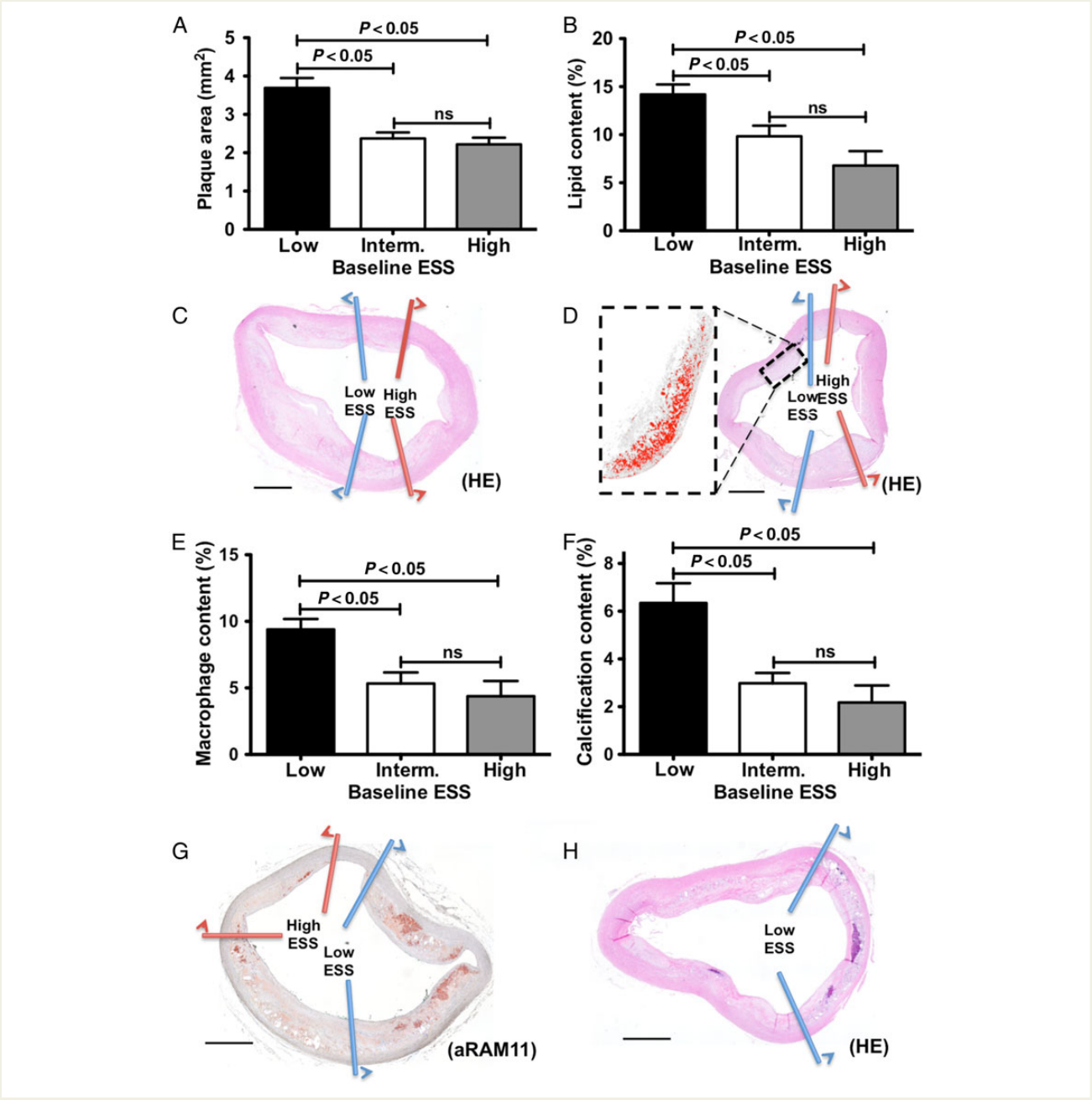

Figure 5 Histopathology analysis and baseline ESS: increased plaque area (*A*), lipid content (*B*), macrophage accumulation (*E*), and calcium content (*F*) in subsegments with low baseline ESS compared with intermediate or high ESS. Representative images of haematoxylin–eosin (*C*, *D*, and *H*) and anti-RAM-11 immunostaining for inflammation (*G*). Magnification of lipid-rich area is shown in (*D*); bars represent 1000 μm.

associated significantly with non-calcified plaque area by CTA ($y = 1.95x - 1.26$, $P < 0.001$) and with macrophage content determined histopathologically ($y = 13.37x - 8.30$, $P < 0.001$; *Figure 6A*), showing that NER accurately tracks plaque inflammation. Using a ROC-adjusted cut-off value of macrophage density >5.3% to differentiate between macrophage-rich vs. macrophage-poor plaque, ROC-analysis identified a NER value at follow-up of ≥1.23 to be highly associated with macrophage-rich plaques (AUC = 0.989; 95% CI 0.933–1.00; $P < 0.0001$). Non-calcified plaque area in CTA correlated well with macrophage content measured immunohistochemically ($y = 4.51x + 2.38$, $P < 0.001$, *Figure 6B*). At baseline, low ESS subsegments co-localized with significantly higher NER compared with that co-localized with higher ESS subsegments (*Figure 6C*). NER increased significantly from baseline to follow-up in subsegments with low baseline ESS compared with regions with intermediate or high baseline ESS (ΔNER: 20.5 ± 4.0 vs. 2.4 ± 3.9 vs. 3.4 ± 4.9%, $P = 0.003$ for low vs. intermediate ESS and for low vs. high ESS; *Figure 6D* and *E*). The increase in NER in areas with low baseline ESS exceeded the intra- and inter-observer variability of NER measurements (1.9 ± 1.3 and 2.8 ± 4.3%,

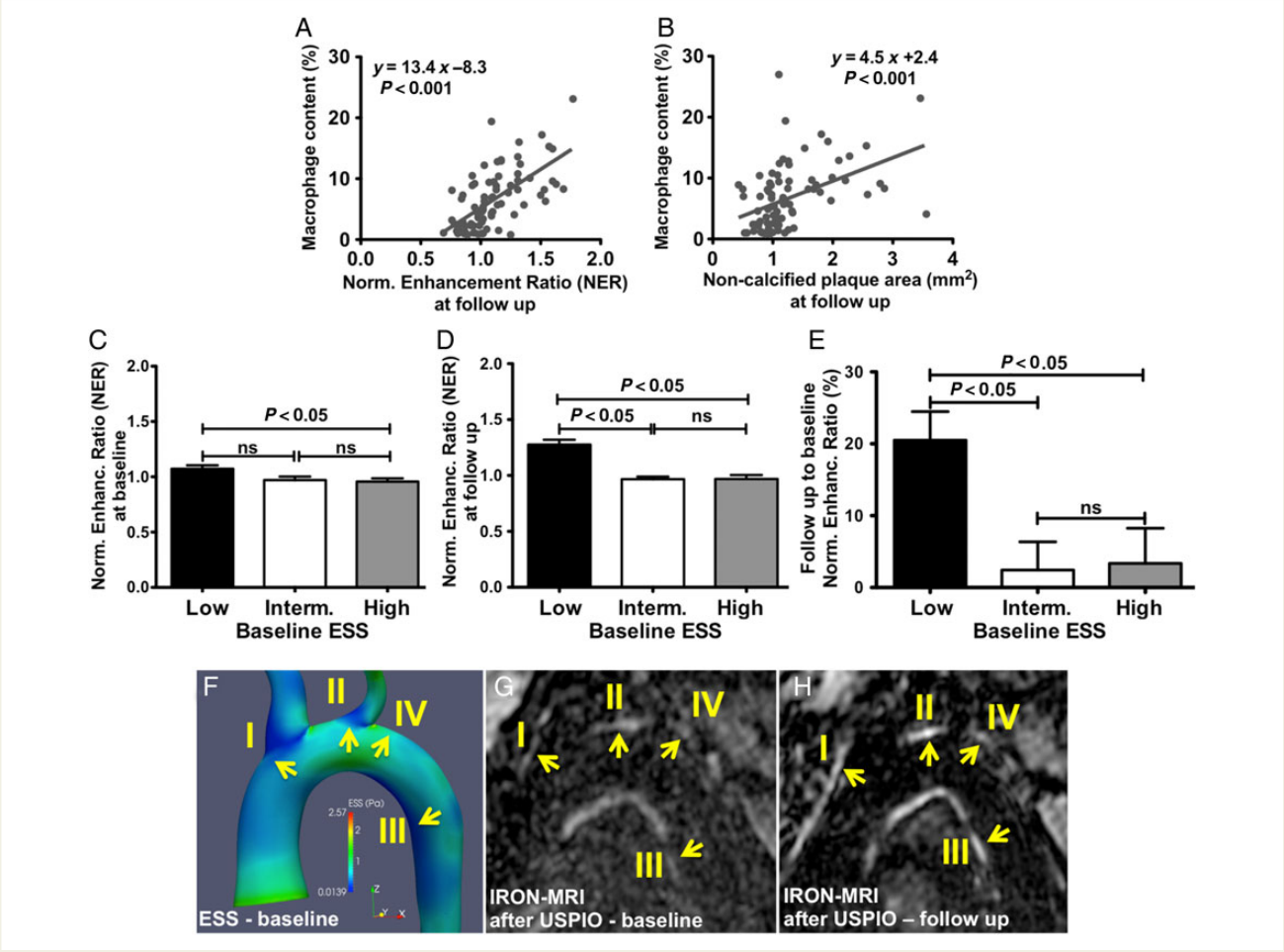

Figure 6 Wall inflammation by USPIO-enhanced IRON-MRI and ESS: association of macrophage content by immunostaining with plaque inflammation measured as NER by USPIO-enhanced IRON-MRI (*A*) and with non-calcified plaque area by CTA (*B*). Subsegments with low ESS at baseline exhibited increased NER values at baseline (*C*) and follow-up (*D*) and increased progression of NER compared with low or intermediate ESS (*E*). Representative example depicting increased wall inflammation (NER) (*G* and *H*) in subsegments with low baseline ESS (I–III) vs. subsegments with high ESS (IV) (*F*).

respectively). *Figure 6F–H* shows a representative example of NER progression in convex and concave subsegments with low baseline ESS.

Figure 7A–K shows a non-calcified plaque by CTA, with co-localized elevated NER in USPIO-enhanced IRON-MRI (*Figure 7G* and *J*), and increased accumulation of inflammatory cells determined histopathologically (*Figure 7H* and *K*). This plaque developed in a convex wall subsegment of the arch with low ESS at baseline (*Figure 7A*). In contrast, an aortic subsegment with high baseline ESS (*Figure 7B*) showed no evidence of plaque by CTA (*Figure 7C*), with no NER in USPIO-enhanced IRON-MRI (*Figure 7D*), and absence of plaque by histopathology (*Figure 7E*).

Baseline predictors of plaque progression, inflammation progression, and high-risk plaque features

Multiple regression analysis showed that low ESS and NER at baseline independently predict wall thickness increase by MRI ($R^2 = 0.20$), non-calcified plaque progression by CTA ($R^2 = 0.35$), inflammation progression (ΔNER) by USPIO-enhanced IRON-MRI ($R^2 = 0.37$), and lipid accumulation ($R^2 = 0.31$) and inflammation by histopathological examination ($R^2 = 0.32$) (*Table 2*). The composite of low ESS and inflammation by USPIO-enhanced IRON-MRI at baseline most strongly predicted plaque inflammation gauged by immunohistopathological study (composite ESS and NER: AUC = 0.89, 95% CI 0.79–0.95, $P < 0.001$; ESS only: AUC = 0.84, 95% CI 0.74–0.91, $P < 0.001$; NER only: AUC = 0.74, 95% CI 0.63–0.84, $P = 0.003$) (*Table 3*).

Inter- and intra-observer agreement

There was excellent inter- and intra-observer agreement for wall thickness by conventional MRI, NER by molecular MRI, and plaque burden by CTA (*Table 4*).

Discussion

This *in vivo* experimental study used serial conventional and USPIO-enhanced IRON-MRI and high-resolution CTA imaging to

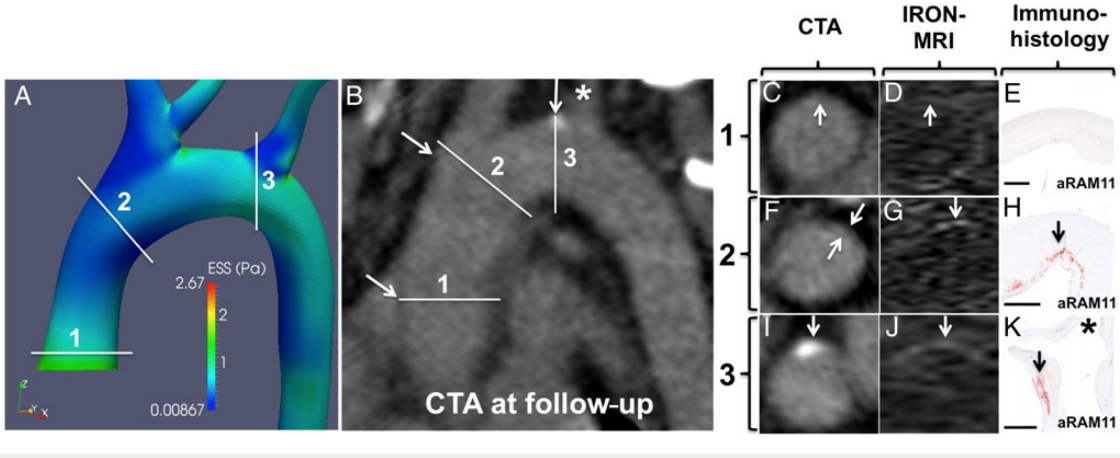

Figure 7 CFD, CTA, contrast MRI, and histopathological validation: (*A*) CFD of a 3D reconstructed aorta showing three convex curvature subsegments with high ESS (1) or low ESS (2 and 3) at baseline. (*B*) Multiplanar reformatting of the aorta by CTA at follow-up. Cross-sectional image of subsegments 1–3 by CTA (*C*, *F*, and *I*), IRON-MRI (*D*, *G*, and *J*), and histopathological examination (*E*, *H*, and *K*, aRAM11; bars represent 1000 μm) showing no plaque in subsegment 1 and inflamed plaque in subsegments 2 and 3. Of note, the asterisks in (*B* and *K*) correspond to the ostium of the left innominate artery.

Table 2 Baseline independent predictors of plaque progression, inflammation progression, and high-risk plaque features

	Non-invasive imaging								
	ΔWall thickness (BB-MRI)			ΔNER (IRON-MRI)			Non-calcified plaque volume (follow-up CTA)		
	$y = ax + \beta$	*r*	*P*	$y = ax + \beta$	*r*	*P*	$y = ax + \beta$	*r*	*P*
Baseline ESS	$-15.6x + 21.9$	−0.33	0.003	$-41.4x + 27.9$	−0.31	0.002	$-2.4x + 2.7$	−0.53	<0.001
Baseline NER	$26.5x - 17.3$	0.38	<0.001	$-59.7x + 67.0$	−0.41	0.001	$1.97x - 1.07$	0.41	0.004
	Histopathology								
	Plaque area			**Lipid content**			**Macrophage content**		
	$y = ax + \beta$	*r*	*P*	$y = ax + \beta$	*r*	*P*	$y = ax + \beta$	*r*	*P*
Baseline ESS	$-2.5x + 4.4$	−0.50	<0.001	$-17.7x + 22.7$	−0.55	<0.001	$-12.7x + 16.6$	−0.53	<0.001
Baseline NER	$1.96x + 0.61$	0.23	0.04	$11.3x - 1.16$	0.22	0.02	$10.6x - 5.3$	0.32	0.003

ESS, endothelial shear stress; NER, normalized enhancement ratio; MRI, magnetic resonance imaging; CTA, computed tomography angiography.

assess plaque changes in the aortas of rabbits with genetic hyperlipidaemia. Histopathological validation demonstrated that (i) low baseline ESS associates with progression of inflamed plaque, and (ii) the combination of low ESS with increased USPIO uptake in IRON-MRI strongly predicts development of inflamed plaque. This proof-of-concept study provides a rationale for future investigations in humans using non-invasive high-resolution imaging and CFD to identify plaques with high-risk characteristics. The ability to predict the development of such plaques non-invasively could facilitate the development of novel therapies to reduce atherosclerotic complications.

Non-invasive assessment of plaque inflammation by USPIO uptake in molecular MRI

Inflammatory burden influences plaque stability and clinical outcomes.[1,27–31] Several strategies strive to assess arterial inflammation and macrophages including soluble biomarkers, and non-invasive and invasive imaging. ^{18}F-FDG PET and targeted PET tracers provide non-invasive approaches for quantitative assessment of plaque inflammation.[29,30] On the other hand, increased USPIO uptake by macrophages reflects their phagocytic activity. The current study

Table 3 Baseline predictors for imaging and histopathology parameters

Parameter	Baseline ESS		Baseline NER		Composite baseline ESS and NER		P
	AUC	95% CI	AUC	95% CI	AUC	95% CI	
By MRI							
ΔWall thickness	0.70	0.59–0.80	0.67	0.56–0.78	0.74	0.63–0.84	<0.001
ΔNER	0.60	0.49–0.71	0.71	0.60–0.81	0.51	0.40–0.63	ns
By CTA							
Non-calcified plaque volume (follow-up)	0.85	0.75–0.92	0.70	0.59–0.80	0.87	0.78–0.94	<0.001
By histopathology							
Plaque area	0.85	0.70–0.89	0.64	0.52–0.82	0.81	0.71–0.89	<0.001
Lipid content	0.71	0.60–0.81	0.61	0.49–0.72	0.73	0.61–0.82	0.02
Macrophage content	0.84	0.74–0.91	0.74	0.63–0.84	0.89	0.79–0.95	<0.001

ESS, endothelial shear stress; NER, normalized enhancement ratio; MRI, magnetic resonance imaging; CTA, computed tomography angiography.

Table 4 Intra- and inter-observer agreement of CTA and MRI morphometric parameters

Parameter	Intra-observer				Inter-observer			
	r	$y = ax + \beta$	Bias (upper, lower limits)	Variability (%)	*r*	$y = ax + \beta$	Bias (upper, lower limits)	Variability (%)
By MRI								
Wall thickness	0.92	$1.0x + 0.0$	0.10 −0.11	1.1 ± 1.8	0.86	$1.3x + 0.3$	0.14 −0.18	1.6 ± 2.0
NER	0.96	$0.9x + 0.1$	0.10 −0.08	1.9 ± 1.3	0.89	$0.64x + 0.4$	0.38 −036	2.8 ± 4.3
By CTA								
Plaque area	0.90	$0.9x + 0.0$	0.92 −1.26	7.2 ± 5.6	0.96	$1.1x - 0.2$	0.88 −1.27	4.7 ± 4.9
Plaque volume	0.96	$0.9x + 0.2$	1.35 −1.22	4.4 ± 5.9	0.95	$1.1x + 0.1$	1.04 −0.69	4.5 ± 6.2

NER, normalized enhancement ratio; MRI, magnetic resonance imaging; CTA, computed tomography angiography.

evaluated the severity of plaque inflammation by application of off-resonance IRON-MRI to assess the signal intensity of USPIO with simultaneous intrinsic background suppression.[32] The use of this particular off-resonance imaging technique instead of traditional T2- or T2*-weighted protocols avoided intensity changes, which could artificially occur from increased free water from inflammation-associated local edema[33,34] or presence of reactive oxygen species.[33] Our findings agree with previous studies showing that high-resolution MRI using USPIOs can identify plaque inflammation and its changes during atherogenesis.[9,10,12,35]

Non-invasive assessment of plaque composition in CTA

CTA can non-invasively characterize and quantify atherosclerotic plaques.[36,37] CTA enables detection and evaluation of serial changes in plaque.[38,39] More recent investigations have linked the severity of plaque inflammation with non-calcified plaque composition by CTA.[40,41] Beyond these observations, the present study used an innovative approach of combined USPIO-enhanced IRON-MRI with high-resolution CTA to detect a significant association of non-calcified plaque burden by CTA with inflammatory burden by USPIO uptake in IRON-MRI and lipid and macrophage content with histomorphometric validation. The results highlight the potential of the multimodality non-invasive imaging to identify inflamed plaques.

Low ESS associates with inflamed plaque

In this study, we evaluated ESS using a combined approach of 2D velocity-encoded PC-MRI for direct measurement of inlet velocities, 3D reconstruction of thoracic aortas derived from CTA, and standardized state-of-the-art software for CFD, yielding reliable and reproducible ESS calculations. Alternatively, ESS could have been derived from time-resolved 3D velocity-encoding PC-MRI of the aorta,[42] which, however, would require dedicated imaging protocols and time-consuming post-processing calculations.

Prior experimental and primarily invasive studies have shown that low ESS promotes atherogenesis and atherosclerotic plaque progression by activating several downstream molecular signalling pathways that regulate lipid accumulation, inflammation, fibrous cap, media thinning, and expansive remodelling.[7,43,44] Our study further demonstrates, using conventional CFD, that low ESS either alone or combined with inflammation imaging by USPIO-enhanced

IRON-MRI in the aortas of hereditary hyperlipidaemic rabbits independently predicts (i) progression of inflammation by USPIO uptake in IRON-MRI, (ii) progression of non-calcified plaque burden by CTA, and (iii) formation of plaques with high-risk features as validated histopathologically. This study combines ESS with non-invasive high-resolution plaque imaging techniques to evaluate the role of ESS in influencing the natural history of atherosclerosis and formation of plaques with high-risk features.

Study limitations

This study has several limitations. First, MRI and CTA had different spatial resolution, due in part to the lengthy imaging time for MRI and anaesthesia duration. Plaque and vessel area were not assessed in BB-TFE-MRI due to low through-plane resolution. This study required meticulous co-registration of imaging, CFD, and histopathology performed using anatomical landmarks in both the longitudinal and circumferential dimensions. The assumption of laminar flow for our modelling approach may bear aberrations from real flow conditions in certain vascular territories, e.g. branch points. The study population was limited ($n = 12$ rabbits); however, investigating multiple convex and concave wall subsegments of interest ($n = 85$, after exclusion of 3 segments) significantly increased the power of the study. This study's design and primary purpose probed the role of different patterns of local ESS in atherosclerosis progression by non-invasive imaging therefore obviating the need for non-atherosclerotic controls. Subsegments with higher ESS and negative features by histopathology served as internal controls. We substantially minimized the longitudinal and circumferential heterogeneity within the aorta by selecting 5-mm-long convex and concave wall subsegments of interest. Finally, H&E-stained sections evaluated the lipid core area of plaques. The paraffin embedding used to preserve the geometry of the perfusion fixed tissues did not permit Oil red O staining.

Conclusion

Serial IRON-MRI in conjunction with USPIOs and high-resolution CTA identified accelerated plaque progression and inflammation progression at 6 months in aortic subsegments of hyperlipidaemic rabbits with low baseline ESS. Non-invasive assessment of local ESS in combination with inflammation affirms the mechanistic link between low ESS and plaque evolution and inflammation. The application of these results has considerable potential to guide therapy and speed the evaluation of novel therapies for atherosclerosis. The findings of this proof-of-concept experimental study now warrant further validation in man.

Supplementary data

Supplementary data are available at *European Heart Journal – Cardiovascular Imaging* online.

Acknowledgements

The authors thank Dr Andreas Giannopoulos for his contribution in the preparation of *Figure 2*.

Conflicts of interest: None declared.

Funding

This work was funded by MSD (grant 3909) and Ernst and Berta Grimmke Foundation (grant 1/12) to G.G. and G.K.; Behrakis Foundation, Boston, MA, USA to Y.S.C. and A.P.A.; European Commission, Framework Program 7, Marie Curie International Reintegration Grant, Project: SMILE (grant 249303) to Y.S.C.; and National Institutes of Health, National Institute of Biomedical Imaging and Bioengineering (grant number K01-EB015868) to D.M.

References

1. Libby P. Inflammation in atherosclerosis. *Nature* 2002;**420**:868–74.
2. Libby P, Tabas I, Fredman G, Fisher EA. Inflammation and its resolution as determinants of acute coronary syndromes. *Circ Res* 2014;**114**:1867–79.
3. Back M, Hansson GK. Anti-inflammatory therapies for atherosclerosis. *Nat Rev Cardiol* 2015;**12**:199–211.
4. Fayad ZA, Fuster V. Clinical imaging of the high-risk or vulnerable atherosclerotic plaque. *Circ Res* 2001;**89**:305–16.
5. Tunick PA, Kronzon I. Atheromas of the thoracic aorta: clinical and therapeutic update. *J Am Coll Cardiol* 2000;**35**:545–54.
6. Chatzizisis YS, Coskun AU, Jonas M, Edelman ER, Feldman CL, Stone PH. Role of endothelial shear stress in the natural history of coronary atherosclerosis and vascular remodeling: molecular, cellular, and vascular behavior. *J Am Coll Cardiol* 2007;**49**:2379–93.
7. Chatzizisis YS, Baker AB, Sukhova GK, Koskinas KC, Papafaklis MI, Beigel R *et al.* Augmented expression and activity of extracellular matrix-degrading enzymes in regions of low endothelial shear stress colocalize with coronary atheromata with thin fibrous caps in pigs. *Circulation* 2011;**123**:621–30.
8. Phinikaridou A, Hua N, Pham T, Hamilton JA. Regions of low endothelial shear stress colocalize with positive vascular remodeling and atherosclerotic plaque disruption: an in vivo magnetic resonance imaging study. *Circ Cardiovasc Imaging* 2013;**6**:302–10.
9. Korosoglou G, Weiss RG, Kedziorek DA, Walczak P, Gilson WD, Schar M *et al.* Noninvasive detection of macrophage-rich atherosclerotic plaque in hyperlipidemic rabbits using "positive contrast" magnetic resonance imaging. *J Am Coll Cardiol* 2008;**52**:483–91.
10. Skinner MP, Yuan C, Mitsumori L, Hayes CE, Raines EW, Nelson JA *et al.* Serial magnetic resonance imaging of experimental atherosclerosis detects lesion fine structure, progression and complications in vivo. *Nat Med* 1995;**1**:69–73.
11. McConnell MV, Aikawa M, Maier SE, Ganz P, Libby P, Lee RT. MRI of rabbit atherosclerosis in response to dietary cholesterol lowering. *Arterioscler Thromb Vasc Biol* 1999;**19**:1956–9.
12. Morishige K, Kacher DF, Libby P, Josephson L, Ganz P, Weissleder R *et al.* High-resolution magnetic resonance imaging enhanced with superparamagnetic nanoparticles measures macrophage burden in atherosclerosis. *Circulation* 2010;**122**:1707–15.
13. Ruehm SG, Corot C, Vogt P, Kolb S, Debatin JF. Magnetic resonance imaging of atherosclerotic plaque with ultrasmall superparamagnetic particles of iron oxide in hyperlipidemic rabbits. *Circulation* 2001;**103**:415–22.
14. Schmitz SA, Taupitz M, Wagner S, Coupland SE, Gust R, Nikolova A *et al.* Iron-oxide-enhanced magnetic resonance imaging of atherosclerotic plaques: postmortem analysis of accuracy, inter-observer agreement, and pitfalls. *Invest Radiol* 2002;**37**:405–11.
15. Taupitz M, Schnorr J, Abramjuk C, Wagner S, Pilgrimm H, Hunigen H *et al.* New generation of monomer-stabilized very small superparamagnetic iron oxide particles (VSOP) as contrast medium for MR angiography: preclinical results in rats and rabbits. *J Magn Reson Imaging* 2000;**12**:905–11.
16. Kiessling F, Huppert J, Zhang C, Jayapaul J, Zwick S, Woenne EC *et al.* RGD-labeled USPIO inhibits adhesion and endocytotic activity of alpha v beta3-integrin-expressing glioma cells and only accumulates in the vascular tumor compartment. *Radiology* 2009;**253**:462–9.
17. Zhang C, Jugold M, Woenne EC, Lammers T, Morgenstern B, Mueller MM *et al.* Specific targeting of tumor angiogenesis by RGD-conjugated ultrasmall superparamagnetic iron oxide particles using a clinical 1.5-T magnetic resonance scanner. *Cancer Res* 2007;**67**:1555–62.
18. Achenbach S, Moselewski F, Ropers D, Ferencik M, Hoffmann U, MacNeill B *et al.* Detection of calcified and noncalcified coronary atherosclerotic plaque by contrast-enhanced, submillimeter multidetector spiral computed tomography: a segment-based comparison with intravascular ultrasound. *Circulation* 2004;**109**:14–7.
19. Achenbach S, Ropers D, Hoffmann U, MacNeill B, Baum U, Pohle K *et al.* Assessment of coronary remodeling in stenotic and nonstenotic coronary atherosclerotic lesions by multidetector spiral computed tomography. *J Am Coll Cardiol* 2004;**43**:842–7.

20. Voros S, Rinehart S, Qian Z, Joshi P, Vazquez G, Fischer C *et al.* Coronary atherosclerosis imaging by coronary CT angiography: current status, correlation with intravascular interrogation and meta-analysis. *JACC Cardiovasc Imaging* 2011;**4**: 537–48.
21. Hoffmann U, Moselewski F, Nieman K, Jang IK, Ferencik M, Rahman AM *et al.* Noninvasive assessment of plaque morphology and composition in culprit and stable lesions in acute coronary syndrome and stable lesions in stable angina by multidetector computed tomography. *J Am Coll Cardiol* 2006;**47**:1655–62.
22. Bamberg F, Sommer WH, Hoffmann V, Achenbach S, Nikolaou K, Conen D *et al.* Meta-analysis and systematic review of the long-term predictive value of assessment of coronary atherosclerosis by contrast-enhanced coronary computed tomography angiography. *J Am Coll Cardiol* 2011;**57**:2426–36.
23. Gitsioudis G, Schussler A, Nagy E, Maurovich-Horvat P, Buss SJ, Voss A *et al.* Combined assessment of high-sensitivity troponin T and noninvasive coronary plaque composition for the prediction of cardiac outcomes. *Radiology* 2015;**276**:73–81.
24. Motoyama S, Sarai M, Harigaya H, Anno H, Inoue K, Hara T *et al.* Computed tomographic angiography characteristics of atherosclerotic plaques subsequently resulting in acute coronary syndrome. *J Am Coll Cardiol* 2009;**54**:49–57.
25. Etienne A, Botnar RM, Van Muiswinkel AM, Boesiger P, Manning WJ, Stuber M. 'Soap-Bubble' visualization and quantitative analysis of 3D coronary magnetic resonance angiograms. *Magn Reson Med* 2002;**48**:658–66.
26. Amirbekian V, Lipinski MJ, Briley-Saebo KC, Amirbekian S, Aguinaldo JG, Weinreb DB *et al.* Detecting and assessing macrophages in vivo to evaluate atherosclerosis noninvasively using molecular MRI. *Proc Natl Acad Sci USA* 2007;**104**: 961–6.
27. Shah PK. Mechanisms of plaque vulnerability and rupture. *J Am Coll Cardiol* 2003; **41**(Suppl. S):15S–22S.
28. Virmani R, Burke AP, Farb A, Kolodgie FD. Pathology of the vulnerable plaque. *J Am Coll Cardiol* 2006;**47**(Suppl.):C13–8.
29. Joshi NV, Vesey AT, Williams MC, Shah AS, Calvert PA, Craighead FH *et al.* 18F-fluoride positron emission tomography for identification of ruptured and high-risk coronary atherosclerotic plaques: a prospective clinical trial. *Lancet* 2014;**383**: 705–13.
30. Tarkin JM, Joshi FR, Rudd JH. PET imaging of inflammation in atherosclerosis. *Nat Rev Cardiol* 2014;**11**:443–57.
31. Randolph GJ. Emigration of monocyte-derived cells to lymph nodes during resolution of inflammation and its failure in atherosclerosis. *Curr Opin Lipidol* 2008;**19**: 462–8.
32. Stuber M, Gilson WD, Schar M, Kedziorek DA, Hofmann LV, Shah S *et al.* Positive contrast visualization of iron oxide-labeled stem cells using inversion-recovery with ON-resonant water suppression (IRON). *Magn Reson Med* 2007;**58**:1072–7.
33. Noseworthy MD, Bray TM. Effect of oxidative stress on brain damage detected by MRI and in vivo 31P-NMR. *Free Radic Biol Med* 1998;**24**:942–51.
34. Denis MC, Mahmood U, Benoist C, Mathis D, Weissleder R. Imaging inflammation of the pancreatic islets in type 1 diabetes. *Proc Natl Acad Sci USA* 2004;**101**: 12634–9.
35. Corti R, Osende JI, Fallon JT, Fuster V, Mizsei G, Jneid H *et al.* The selective peroxisomal proliferator-activated receptor-gamma agonist has an additive effect on plaque regression in combination with simvastatin in experimental atherosclerosis: in vivo study by high-resolution magnetic resonance imaging. *J Am Coll Cardiol* 2004; **43**:464–73.
36. Maurovich-Horvat P, Ferencik M, Voros S, Merkely B, Hoffmann U. Comprehensive plaque assessment by coronary CT angiography. *Nat Rev Cardiol* 2014;**11**:390–402.
37. Korosoglou G, Mueller D, Lehrke S, Steen H, Hosch W, Heye T *et al.* Quantitative assessment of stenosis severity and atherosclerotic plaque composition using 256-slice computed tomography. *Eur Radiol* 2010;**20**:1841–50.
38. Aziz K, Berger K, Claycombe K, Huang R, Patel R, Abela GS. Noninvasive detection and localization of vulnerable plaque and arterial thrombosis with computed tomography angiography/positron emission tomography. *Circulation* 2008;**117**: 2061–70.
39. Ibanez B, Cimmino G, Benezet-Mazuecos J, Santos-Gallego CG, Pinero A, Prat-Gonzalez S *et al.* Quantification of serial changes in plaque burden using multidetector computed tomography in experimental atherosclerosis. *Atherosclerosis* 2009;**202**:185–91.
40. Hyafil F, Cornily JC, Rudd JH, Machac J, Feldman LJ, Fayad ZA. Quantification of inflammation within rabbit atherosclerotic plaques using the macrophage-specific CT contrast agent N1177: a comparison with 18F-FDG PET/CT and histology. *J Nucl Med* 2009;**50**:959–65.
41. Hur J, Kim YJ, Shim HS, Lee HJ, Nam JE, Choe KO *et al.* Assessment of atherosclerotic plaques in a rabbit model by delayed-phase contrast-enhanced CT angiography: comparison with histopathology. *Int J Cardiovasc Imaging* 2012;**28**:353–63.
42. Stalder AF, Russe MF, Frydrychowicz A, Bock J, Hennig J, Markl M. Quantitative 2D and 3D phase contrast MRI: optimized analysis of blood flow and vessel wall parameters. *Magn Reson Med* 2008;**60**:1218–31.
43. Platt MO, Ankeny RF, Shi GP, Weiss D, Vega JD, Taylor WR *et al.* Expression of cathepsin K is regulated by shear stress in cultured endothelial cells and is increased in endothelium in human atherosclerosis. *Am J Physiol Heart Circ Physiol* 2007;**292**: H1479–86.
44. Sun HW, Li CJ, Chen HQ, Lin HL, Lv HX, Zhang Y *et al.* Involvement of integrins, MAPK, and NF-kappaB in regulation of the shear stress-induced MMP-9 expression in endothelial cells. *Biochem Biophys Res Commun* 2007;**353**:152–8.